Frenkel Defects Promote Polaronic Exciton Dissociation in Methylammonium Lead Iodide Perovskites

Journal:	*Physical Chemistry Chemical Physics*
Manuscript ID	CP-ART-01-2021-000222.R2
Article Type:	Paper
Date Submitted by the Author:	18-Feb-2021
Complete List of Authors:	Guan, Yuhan; Zhejiang Normal University, Department of Physics Zhang, Xu; California State University Northridge, Physics and Astronomy Nan, Guangjun; Zhejiang Normal Univeristy, Department of Physics

Frenkel Defects Promote Polaronic Exciton Dissociation in Methylammonium Lead Iodide Perovskites

Yuhan Guan,[1] Xu Zhang,[2] Guangjun Nan[1*]

[1] Department of Physics, Zhejiang Normal University, Jinhua, Zhejiang 321004, P. R. China

[2] Department of Physics and Astronomy, California State University, Northridge, Northridge, California 91330- 8268, United States

*Corresponding author

gjnan@zjnu.edu.cn

Abstract

Hybrid organic-inorganic perovskite materials, such as $CH_3NH_3PbI_3$, exhibit substantial potentials in a variety of optoelectronic applications. Nevertheless, the interplay between the photo-induced excitations and iodine Frenkel defects which are abundant in $CH_3NH_3PbI_3$ films remains poorly understood. Here we study the light-triggered electronic and excitonic properties in the presence of iodine Frenkel defects in $CH_3NH_3PbI_3$ by using a combination of density functional theory (DFT) and time-dependent DFT approaches, the latter of which treats electron-hole and electron-nuclei interactions on the same footing. For isolated Frenkel defects, electrons are trapped close to the iodine vacancies and electron-hole correlation brings the holes in close vicinity to the electrons, yielding tightly bound polaronic excitons. However, in presence of multiple interactive Frenkel defects, the holes are pulled out from electron-hole Coulomb well by the iodine interstitials, leading to spatially separated electron-hole pairs. The X-ray photoelectron spectroscopy are then simulated, unravelling the light-triggered charge transfer induced by Frenkel defects at the atomistic level. We also find that the energy and spatial distributions of polaronic excitons at the Frenkel defect can be controlled by the dynamical rotation of organic cations.

1. Introduction

Hybrid organic-inorganic perovskite (HOIP) materials are drawing attention in photovoltaic application owing to the rapid rise of power conversion efficiency.[1-2] To date, HOIPs have achieved a certified power conversion efficiency exceeding 25%.[3] The impressive performances of this class of materials are enabled by a unique combination of desired properties, including high optical absorption coefficient, high carrier mobility and low electron-hole (e-h) binding energies.[4] Remarkably, the long carrier lifetime and diffusion length have been reported in solution-processed HOIPs,[5-7] e.g., the methylammonium lead iodide ($MAPbI_3$ with $MA=CH_3NH_3^+$) which can bear trap densities up to 10^{17}~10^{18} cm^3.[8-9] This is sharply contrast to the picture of a typical semiconductor which shows rather limited carrier lifetime and diffusion length owing to the scattering at defects or impurities. To complete the picture, researchers require an accurate understanding of the nature of the carriers and the role played by defects in the photophysics of HOIPs.

Significant effort has been devoted to the study of high defect tolerance of HOIPs.[4] Several studies indicate a significant probability for the formation of native defects in $MAPbI_3$, but most typical point defects introduce shallow trap states (i.e. electronic states lying close to the band-edges, comparable to or less than the available thermal energy).[10-12] Electron-phonon coupling coupled with long-range Coulomb potentials give rise to large polarons as a result of extended lattice distortion.[13] Such polaron formation can protect the photogenerated electrons and holes from recombination and defect-scattering. These would explain the limited impact of defects on solar cell performance. Nevertheless, non-negligible channels of electron and energy losses are experimentally resolved, suggesting the presence of fairly deep trap states.[14-15] These deep in-gap energy levels may arise from the small polarons which originate from localized lattice reorganizations induced corporately by both inorganic lattice distortion and organic cation rotations.[16] It is worth noting that the defect-related lattice distortion can be triggered by the photoexcitation,[17-18] transforming large polaron (shallow traps) in dark to small polaronic exciton (discrete in-gap traps) in excited states.[19-20] shedding light on the significant role of exciton-defect interactions on determining the nature of defects in HOIPs. This is consistent with photoluminescence and spectroscopy measurements that suggest non-trivial e-h recombination,[21-23] in particular for HOIPs with non-stoichiometric chemical compositions.[24-27]

So far, a considerable amount of research has been directed to focus on native point defects such as vacancy defect and interstitial defect for iodine elements in $MAPbI_3$.[10, 28-29] Unlike conventional semiconducting materials, however, $MAPbI_3$ bear strong ionic bonding features,[30] so the defects composed of neutral anion-cation pairs should be considered. Defect migration due to ion diffusion could be the source of Frenkel defects (FDs) which consist of a positively charged vacancy defect and a negatively charged interstitial defect.[31] To the best of our knowledge, very limited studies have been performed to mainly focus on the activation barriers of Frenkel pairs in HOIPs,[32-34] so further studies on the properties of FDs are largely demanded. Notably, with the help of high-resolution X-ray photoelectron spectroscopy (XPS) technique, an obvious shift of iodine 3d and lead 4f core-level energies has been experimentally resolved in $MAPbI_3$ films under light irradiation, whereas the core-level spectra before and after light illumination are hardly affected in $MAPbI_3$ single crystals.[35] Such contrast behaviors in $MAPbI_3$ films and single crystals demands a careful exploration towards the photophysical properties of FDs in $MAPbI_3$.

Iodine-related defects exhibit low formation energies and migration barriers,[12, 36] so the negatively charged iodine interstitial (I_i^-) and positively charged iodine vacancy (V_I^+) pairs are relatively abundant in $MAPbI_3$ films as supported by experiments.[21] Here, we sought to combine density functional theory

(DFT) and time-dependent DFT (TDDFT) approaches to study the behavior of $MAPbI_3$ in presence of iodine FDs. We show the spatial extent of photogenerated e-h pairs in $MAPbI_3$ with one isolated iodine FD, labeled as $MAPbI_3$-FD1, and two interactive iodine FDs, referred to as $MAPbI_3$-FD2. These results are also compared with those of $MAPbI_3$ with iodine point defects, which provides a deep insight of FDs to the e-h dissociation and electron transfer in $MAPbI_3$ films.

2. Computational details

While the $MAPbI_3$ in tetragonal phase is stable at room temperature,[37] the $MAPbI_3$ in cubic phase are adopted in this work based on the considerations below. Firstly, the theoretical calculations suggested that the properties of traps are not affected by crystalline phases.[12, 20, 38] Secondly, the lattice parameters of the 4×4×4 supercells in cubic phase (a=6.33 Å) are larger than the screening radius (~0.8 nm) around a point defect,[39] so the interactions between the native point defects and their images are largely negligible. Thirdly, the screening distance between different Frenkel defects is enlarged as much as possible to weaken their interactions. Fixing the cell parameters of the cubic crystalline phase,[40] the primitive cell is periodically expanded, generating a 4×4×4 supercell (namely 64 $MAPbI_3$ units) with 768 ions in paraelectric configuration where the MA cations have random orientation in the supercell. One or two Frenkel defects are then created in different spatial domains. Based on the projected augmented wave pseudopotentials and the Perdew-Burke-Ernzerhof (PBE) functional, the ground-state geometric optimization is carried out by using DFT approach with a plane-wave basis set, as implemented in Vienna ab initio simulation package (VASP).[41] The valence electrons of 4, 7, 4, 5 and 1 are treated for atoms of Pb, I, C, N and H species, respectively. All the DFT calculations are performed with a cutoff energy of 400 eV at the Γ point which has been shown to be sufficient in predicting the band gap and defective properties for the lead halide perovskites.[11] The convergence criteria for energy and forces are set to be 10^{-4} eV and 0.04 eV/Å, respectively. Based on the fully optimized ground-state geometries, a recently developed large-scale TDDFT approach is employed to assess the photo-induced excited-state geometries and primary excitations.[42] In this scheme, the ionic forces and charge densities in the excited state are calculated by the derivatives of the Lagrangian functional with respect to ionic position and external potential, respectively. In both the ground-state and excited-state calculations, the semi-empirical DFT-D2 method is used to account for the van der Waals corrections.[43] Since the reasonable band gap produced by the PBE functional originates from a cancelation of two effects, namely the lack of spin-orbital interactions and the self-interaction error inherent to pure DFT functionals,[44] the results by PBE functional are validated by carrying out calculations including spin-orbital coupling (SOC) corrections and applying an optimally-tuned range-separated hybrid (OT-RSH) functional.[45] In order to reproduce the fundamental band gap from the GW calculations,[46-47] the range-separation parameter is set to be zero which has been used in our recent work for $MAPbI_3$.[20] The XPS core level energies of ions in both the ground-state and excited-state geometries are simulated with the initial-state approach,[48] which is performed in VASP by recalculating the Kohn-Sham eigenvalues of the core states subsequent to the self-consistent determination of the charge density associated with the valence electrons.[49]

3. Results and Discussion

It is noted that a tightly bound I_i^-/V_I^+ pair could dissociate via successive diffusion of iodine ions,[32] but the iodine ion diffusion is complicated by coupling with the orientational MA cations which happens in sub-picosecond.[50-51] Hence, the mechanism of iodine ion diffusion in $MAPbI_3$ is beyond the scope of this work. For simplicity, we study paraelectric $MAPbI_3$-FD1 which holds spatially separated I_i^-/V_I^+ pair (Figure 1a). While the concentration of the iodine FDs is as high as 10^{19}~10^{20}

cm^{-3} in this work, Walsh *et al.* have suggested the defect concentrations in $MAPbI_3$ can reach this level.[52] At any given "instantaneous" configuration for which the MA ions are static, the electronic excitation in the ground-state configuration is delocalized (Figure 1b), yielding both shallow hole and electron trap states as supported by the density of states (DOS) (Figure 1d). In the excited-state geometry, however, the electronic excitation turns to be rather localized in the vicinity of V_I^+ defect (Figure 1c). A discrete in-gap electron trap resolved in the excited state (Figure 1d) originates from the local geometric deformation (Figure 1e) in the vicinity of the V_I^+ defect (Figure 1f) when comparing the ground-state and excited-state geometries. Due to the Coulomb attraction between the photogenerated e-h pair, the holes are trapped by the electrons in the trap, forming a tightly bound polaronic exciton surrounding the V_I^+ defect. We note that the I_i^- defect itself has marginally effect on the charge localization (Figures S1a and S1b), whereas the V_I^+ defect itself promotes the crossover of charge densities from the spatial extension to local confinement (Figures S1c and S1d).[20] Therefore, the tightly bound polaronic exciton in the excited state is induced by the V_I^+ defect.

Since the dipolar MA cations can affect the charge distributions in the vicinity of defects by interacting with the inorganic lattice,[53] the effect of the dynamical MA cations on the nature of the e-h pairs is explored by reorienting the first neighboring MA cations surrounding the I_i^- and V_I^+ defects, respectively. In the case of $MAPbI_3$-FD1 with the I_i^- defect oriented by the nearest -NH_3 moieties, both charge densities and DOS show similar crossover to those in Figure 1 when going from the ground state to the excited state (Figures 2a-2c), yielding a tightly bound polaronic exciton in the excited state. When the I_i^- defect is pointed by the nearest -CH_3 moieties, however, hole densities turn to be slightly confined in the ground state (Figure 2d) and becomes rather localized in the excited state (Figure 2e). In this case, the e-h pair gets separated in the excited state and both hole and electron in-gap traps are resolved (Figure 2f). Due to the attractive (repulsive) interactions between the positively (negatively) charged -NH_3 (-CH_3) groups and I_i^- defect, the former case is ~15 meV/nm^{-3} smaller than the latter case in the excited state, indicating the tightly bound polaronic exciton is preferably formed. In the case of $MAPbI_3$-FD1 with the V_I^+ defect oriented by the nearest -NH_3 groups, the $MAPbI_3$-FD1 show similar charge distribution (Figures 3a and 3b) and DOS (Figure 3c) to those in Figure 1. By contrast, the reversed MA cations closely surrounding the V_I^+ defect, namely the -CH_3 groups oriented towards the V_I^+ defect, prompts the spatially extended charge densities (Figures 3d and 3e); concurrently, the discrete in-gap trap cannot be resolved in the excited state (Figure 3f). The excited-state energy of the latter configuration is energetically ~20 meV/nm^{-3} smaller than the former configuration because of the attractive (repulsive) interactions between the negatively (positively) charged -CH_3 (-NH_3) groups and V_I^+ vacancy. This is in line with our recent work that the deep electron traps (Figures 1c and 1d) could be healed by the reorientation of MA cations. Taken together, the tightly bound polaronic exciton formed in paraelectric $MAPbI_3$-FD1 is largely controlled by the electrostatics between the dipolar MA cations and the charged native point defects.

We then move to $MAPbI_3$-FD2 by generating an iodine FD in $MAPbI_3$-FD1. The two iodine FDs in $MAPbI_3$-FD2 are interactive by keeping their distance smaller than the screening radius (~0.8 nm),[39] so the change of defect properties in $MAPbI_3$-FD2 with respect to $MAPbI_3$-FD1 is contributed by the newly created Frenkel pair. It is noted that, when the iodine ion of the second Frenkel pair is close to the iodine ion of the first Frenkel pair, the I_i^- defect in $MAPbI_3$-FD1 moves to an adjacent inorganic cavity (Figure 4a), indicating the correlation of the relative positions of iodine ions owing to their repulsive interactions. In analogy to $MAPbI_3$-FD1, the delocalized electronic excitation in the ground state is sustained (Figures 4b and 4d). Very strikingly, however, $MAPbI_3$-FD2 in the excited state exhibits spatially separated hole-rich and electron-rich domains (Figure 4c), which is sharply different from the case in $MAPbI_3$-FD1 which confine both holes and electrons in the vicinity of V_I^+ defect. We verify that regardless of the position of I_i^- defects (Figure S2a) and V_I^+ defects (Figure S2b) of the second Frenkel pair, a fraction of holes and electrons remain spatially separated (Figures S2c and S2d). These suggest consistently a fraction of holes is pulled out from the V_I^+ defects in the $MAPbI_3$-FD2, manifesting that the second Frenkel pair promotes the e-h separation. The reasons are analyzed as follows. Analogous to $MAPbI_3$-FD1, the ions with largest distortions (Figure 4e) locate in the vicinity of the V_I^+ defects (Figure 4f) when going from the ground state to the excited state. The geometric deformation is thus excluded to contribute to the separated e-h pair. Since the $MAPbI_3$ with two I_i^- defects show spatially extended hole and electron excitation (Figure S3a and S3b) and the $MAPbI_3$ with two V_I^+ defects confine both hole and electron in the vicinity of V_I^+ defects (Figure S3c and S3d), we attribute the spatially confined hole and electron in different domains of $MAPbI_3$-FD2 to the enhanced Coulomb attraction between the two I_i^- ions and hole densities. While the trapped electrons tend to attract holes, the Coulomb interaction between I_i^- ions and hole densities is increased in $MAPbI_3$-FD2 compared to $MAPbI_3$-FD1, thus pulling out the holes from the electron traps. This is supported by the separated e-h pair when the I_i^- defect is oriented by the nearest $-CH_3$ groups of MA cations (Figure 2e). We validate that (i) the discrete in-gap traps in Figures 1 and 4 are not affected by including SOC corrections (Figures S4a and S4d) and by treating the long-range e-h interactions with the OT-RSH functional[45] (Figures S4b and S4e); (ii) The charge distributions predicted by OT-RSH functional (Figures S4c and S4f) differ weakly from those predicted by the PBE functional (Figures 1c and 4c), which is likely due to the large dielectric permittivity (thus strong electrostatic screening) in $MAPbI_3$.[54-55] Therefore, the most important finding in this study is that a multiple of interactive iodine FDs can promote the dissociation of the tightly bound polaronic excitons induced by the isolated iodine FDs in $MAPbI_3$.

Notably, the XPS technique has resolved that the I 3d and Pb 4f core levels exhibit ~0.69 eV energy shifts toward lower binding energy in $MAPbI_3$ films and are marginally affected in $MAPbI_3$ single crystals under light illumination.[35] As the experimentally prepared $MAPbI_3$ single crystals are expected to have much lower trap density as compare to the $MAPbI_3$ films, the $MAPbI_3$-FD1 bearing isolated iodine FDs may correspond to the experimentally prepared $MAPbI_3$ single crystals and the $MAPbI_3$-FD2 which holds interactive iodine FDs may map to the experimentally prepared $MAPbI_3$ films. According to such correspondence, our simulated XPS results are consistent with the experimental findings. When comparing the simulated XPS results between pristine $MAPbI_3$ and $MAPbI_3$-FD1, the binding energies of I 3d and Pb 4f core levels in pristine $MAPbI_3$ are weakly affected in the ground state (Figures 5a and 5b) because a tiny of electrons moves from the ions in the vicinity of V_I^+ defect to the ions surrounding the I_i^- defect (Figure 6a). Since the charge carriers reshuffle upon photoexcitation, a fraction of electrons belonging to the iodine and lead ions in the vicinity of V_I^+ defect is captured by the electron traps (Figure 6b). Therefore, the binding energies of I 3d and Pb 4f core levels show asymmetric variations in the excited state, namely a weak change toward low binding energy and a strong shift toward high binding energy (Figures 5c and 5d). Importantly, the isolated iodine FDs can hardly lower the binding energies of I 3d and Pb 4f core levels, which is in line with the experimentally resolved I 3d and Pb 4f core levels in $MAPbI_3$ single crystal under light irradiation.[35]

The picture changes a lot when focusing on the $MAPbI_3$-FD2. Compared to $MAPbI_3$-FD1, there is a slightly stronger electron redistribution within the inorganic framework for $MAPbI_3$-FD2 in the ground state (Figures 5a and 5b). The electrostatics induce the electron densities from the ions in the vicinities of the two V_I^+ defects to the ions surrounding the two I_i^- defects (Figure 6c). In the excited state, the two V_I^+ defects tend to localize the electrons which could in turn have tendency to attract the holes. However, the electron-rich domain (Figure 6d) contributed by the two I_i^- defects in $MAPbI_3$-FD2 have stronger attraction to the holes than the case in $MAPbI_3$-FD1, so a fraction of holes is pulled out from the electron traps (Figure 4c). Resultantly, the binding energies of I 3d and Pb 4f core levels become significantly lower in the excited state (Figures 5c and 5d) than those in the ground state (Figures 5a and 5b). The ~0.60 eV energy shifts toward lower binging energy (Figures 5c and 5d) are consistent with the experimental findings in $MAPbI_3$ films, implying the experimentally resolved electron transfer may be induced by the interactive iodine FDs.

4. Conclusions

In this work, the $MAPbI_3$ in presence of both isolated and interactive iodine FDs are investigated with the combination of DFT and TDDFT approaches. In $MAPbI_3$ with isolated iodine Frenkel pairs, charge transfer happens weakly in the ground-state geometries from the neighborhood of V_I^+ defects to the neighborhood of I_i^- defects. Upon photoexcitation, substantial geometric distortions are resolved in the vicinity of V_I^+ defects which yields deep in-gap electron traps. The electrons are thus trapped close to the V_I^+ defects, manifested by the increase of binding energies of iodine and lead ions in the vicinity of V_I^+ defects. Owing to the e-h correlation, the holes are pulled to the proximity of the spatially confined electrons in $MAPbI_3$ with isolated iodine FDs, thus forming the tightly bound polaronic excitons. Strikingly, a fraction of holes and electrons become spatially separated in the excited-state geometries of $MAPbI_3$ in presence of interactive iodine FDs, which is ascribed to the stronger Coulomb attraction of I_i^- defects to the holes. Hence, a multiple of FDs could promote the dissociation of the polaronic excitons in defective $MAPbI_3$, providing a plausible explanation for the long carrier lifetime and diffusion length in $MAPbI_3$ films. The photo-induced electron transfer in $MAPbI_3$-FD2 is in line with the changes of I 3d and Pb 4f core levels resolved by XPS technique in $MAPbI_3$ films under light irradiation. Besides, the charge distributions in defective $MAPbI_3$ are largely affected by the dipolar MA cations, suggesting the optoelectronic behavior in defective $MAPbI_3$ is complicated by the electrostatics between defects and the organic cations.

Conflicts of interest

There are no conflicts of interest to declare.

Acknowledgments

The authors thank D. Beljonne (University of Mons) for valuable discussions. This work was supported by the Natural Science Foundation of Zhejiang Province (LY20A040003) as well as Key Research and Development Program of Zhejiang Province (2021C01006). The work at California State University Northridge was supported by the US National Science Foundation (DMR-1828019).

References

1. Z. Li, T. R. Klein, D. H. Kim, M. Yang, J. J. Berry, M. F. A. M. van Hest and K. Zhu, *Nat. Rev. Mater.*, 2018, **3**, 18017.
2. A. K. Jena, A. Kulkarni and T. Miyasaka, *Chem. Rev.*, 2019, **119**, 3036-3103.
3. J. Y. Kim, J.-W. Lee, H. S. Jung, H. Shin and N.-G. Park, *Chem. Rev.*, 2020, **120**, 7867-7918.
4. J. Huang, Y. Yuan, Y. Shao and Y. Yan, *Nat. Rev. Mater.*, 2017, **2**, 17042.
5. G. Xing, N. Mathews, S. Sun, S. S. Lim, Y. M. Lam, M. Grätzel, S. Mhaisalkar and T. C. Sum, *Science*, 2013, **342**, 344-347.
6. D. Shi, V. Adinolfi, R. Comin, M. Yuan, E. Alarousu, A. Buin, Y. Chen, S. Hoogland, A. Rothenberger, K. Katsiev, Y. Losovyj, X. Zhang, P. A. Dowben, O. F. Mohammed, E. H. Sargent and O. M. Bakr, *Science*, 2015, **347**, 519-522.
7. Q. Dong, Y. Fang, Y. Shao, P. Mulligan, J. Qiu, L. Cao and J. Huang, *Science*, 2015, **347**, 967-970.
8. Z. Ni, C. Bao, Y. Liu, Q. Jiang, W.-Q. Wu, S. Chen, X. Dai, B. Chen, B. Hartweg, Z. Yu, Z. Holman and J. Huang, *Science*, 2020, **367**, 1352-1358.
9. D. W. deQuilettes, K. Frohna, D. Emin, T. Kirchartz, V. Bulovic, D. S. Ginger and S. D. Stranks, *Chem. Rev.*, 2019, **119**, 11007-11019.
10. D. Meggiolaro, S. G. Motti, E. Mosconi, A. J. Barker, J. Ball, C. Andrea Riccardo Perini, F. Deschler, A. Petrozza and F. De Angelis, *Energy Environ. Sci.*, 2018, **11**, 702-713.
11. W.-J. Yin, T. Shi and Y. Yan, *J. Phys. Chem. C*, 2015, **119**, 5253-5264.
12. W.-J. Yin, T. Shi and Y. Yan, *Appl. Phys. Lett.*, 2014, **104**, 063903.
13. X. Y. Zhu and V. Podzorov, *J. Phys. Chem. Lett.*, 2015, **6**, 4758-4761.
14. S. D. Stranks, *ACS Energy Lett.,* 2017, **2**, 1515-1525.
15. M. Saba, M. Cadelano, D. Marongiu, F. Chen, V. Sarritzu, N. Sestu, C. Figus, M. Aresti, R. Piras, A. G. Lehmann, C. Cannas, A. Musinu, F. Quochi, A. Mura and G. Bongiovanni, *Nat. Commun.*, 2014, **5**, 5049.
16. A. J. Neukirch, W. Nie, J.-C. Blancon, K. Appavoo, H. Tsai, M. Y. Sfeir, C. Katan, L. Pedesseau, J. Even, J. J. Crochet, G. Gupta, A. D. Mohite and S. Tretiak, *Nano Lett.*, 2016, **16**, 3809-3816.
17. J. F. Galisteo-López, Y. Li and H. Míguez, *J. Phys. Chem. Lett.*, 2016, **7**, 5227-5234.
18. R. Gottesman, L. Gouda, B. S. Kalanoor, E. Haltzi, S. Tirosh, E. Rosh-Hodesh, Y. Tischler and A. Zaban, *J. Phys. Chem. Lett.*, 2015, **6**, 2332-2338.
19. E. T. Hoke, D. J. Slotcavage, E. R. Dohner, A. R. Bowring, H. I. Karunadasa and M. D. McGehee, *Chem. Sci.*, 2015, **6**, 613-617.
20. G. Nan, X. Zhang, M. Abdi-Jalebi, Z. Andaji-Garmaroudi, S. D. Stranks, G. Lu and D. Beljonne, *Adv. Energy Mater.*, 2018, **8**, 1702754.
21. D. W. deQuilettes, W. Zhang, V. M. Burlakov, D. J. Graham, T. Leijtens, A. Osherov, V. Bulović, H. J. Snaith, D. S. Ginger and S. D. Stranks, *Nat. Commun.*, 2016, **7**, 11683.
22. D. W. de Quilettes, S. M. Vorpahl, S. D. Stranks, H. Nagaoka, G. E. Eperon, M. E. Ziffer, H. J. Snaith and D. S. Ginger, *Science*, 2015, **348**, 683-686.
23. F. V. A. Camargo, T. Nagahara, S. Feldmann, J. M. Richter, R. H. Friend, G. Cerullo and F. Deschler, *J. Am. Chem. Soc.*, 2020, **142**, 777-782.
24. W. Zhang, S. Pathak, N. Sakai, T. Stergiopoulos, P. K. Nayak, N. K. Noel, A. A. Haghighirad, V. M. Burlakov, D. W. deQuilettes, A. Sadhanala, W. Li, L. Wang, D. S. Ginger, R. H. Friend

and H. J. Snaith, *Nat. Commun.*, 2015, **6**, 10030.
25. C. Qin, T. Matsushima, T. Fujihara, W. J. Potscavage and C. Adachi, *Adv. Mater.*, 2016, **28**, 466-471.
26. W. S. Yang, B.-W. Park, E. H. Jung, N. J. Jeon, Y. C. Kim, D. U. Lee, S. S. Shin, J. Seo, E. K. Kim, J. H. Noh and S. I. Seok, *Science*, 2017, **356**, 1376-1379.
27. S. T. Birkhold, E. Zimmermann, T. Kollek, D. Wurmbrand, S. Polarz and L. Schmidt-Mende, *Adv. Funct. Mater.*, 2017, **27**, 1604995.
28. W. Li, J. Liu, F.-Q. Bai, H.-X. Zhang and O. V. Prezhdo, *ACS Energy Lett.*, 2017, **2**, 1270-1278.
29. J. Wang, W. Li, W.-J. Yin, *Adv. Mater.*, 2020, **32**, 1906115.
30. H.-S. Kim, S. H. Im and N.-G. Park, *J. Phys. Chem. C*, 2014, **118**, 5615-5625.
31. S. T. Birkhold, J. T. Precht, R. Giridharagopal, G. E. Eperon, L. Schmidt-Mende and D. S. Ginger, *J. Phys. Chem. C*, 2018, **122**, 12633-12639.
32. E. Mosconi, D. Meggiolaro, H. J. Snaith, S. D. Stranks, F. De Angelis, *Energy Environ. Sci.*, 2016, **9**, 3180-3187.
33. W. Ming, S. Chen and M.-H. Du, *J. Mater. Chem. A*, 2016, **4**, 16975-16981.
34. A. Oranskaia, J. Yin, O. M. Bakr, J.-L. Brédas and O. F. Mohammed, *J. Phys. Chem. Lett.*, 2018, **9**, 5474-5480.
35. F.-S. Zu, P. Amsalem, I. Salzmann, R.-B. Wang, M. Ralaiarisoa, S. Kowarik, S. Duhm and N. Koch, *Adv. Optical Mater.*, 2017, **5**, 1700139.
36. D. Meggiolaro, E. Mosconi and F. De Angelis, *ACS Energy Lett.*, 2018, **3**, 447-451.
37. C. C. Stoumpos, C. D. Malliakas and M. G. Kanatzidis, *Inorg. Chem.*, 2013, **52**, 9019-9038.
38. A. Buin, R. Comin, J. Xu, A. H. Ip and E. H. Sargent, *Chem. Mater.*, 2015, **27**, 4405-4412.
39. I. Anusca, S. Balčiūnas, P. Gemeiner, Š. Svirskas, M. Sanlialp, G. Lackner, C. Fettkenhauer, J. Belovickis, V. Samulionis, M. Ivanov, B. Dkhil, J. Banys, V. V. Shvartsman and D. C. Lupascu, *Adv. Energy Mater.*, 2017, **7**, 1700600.
40. A. Poglitsch and D. Weber, *J. Chem. Phys.*, 1987, **87**, 6373-6378.
41. G. Kresse and J. Furthmuller, *Phys. Rev. B*, 1996, **54**, 11169-11186.
42. X. Zhang and G. Lu, *J. Chem. Phys.*, 2015, **143**, 064110.
43. S. Grimme, *J. Comput. Chem.*, 2006, **27**, 1787-1799.
44. M.-H. Du, *J. Phys. Chem. Lett.*, 2015, **6**, 1461-1466.
45. S. Refaely-Abramson, M. Jain, S. Sharifzadeh, J. B. Neaton and L. Kronik, *Phys. Rev. B*, 2015, **92**, 081204(R).
46. M. R. Filip and F. Giustino, *Phys. Rev. B*, 2014, **90**, 245145.
47. P. Umari, E. Mosconi and F. De Angelis, *Sci. Rep.*, 2014, **4**, 4467.
48. T. C. Taucher, I. Hehn, O. T. Hofmann, M. Zharnikov and E. Zojer, *J. Phys. Chem. C*, 2016, **120**, 3428-3437.
49. L. Köhler and G. Kresse, *Phys. Rev. B*, 2004, **70**, 165405.
50. E. Mosconi and F. De Angelis, *ACS Energy Lett.*, 2016, **1**, 182-188.
51. C.-J. Tong, W. Geng, O. V. Prezhdo and L.-M. Liu, *ACS Energy Lett.*, 2017, **2**, 1997-2004.
52. A. Walsh, D. O. Scanlon, S. Chen, X. G. Gong and S.-H. Wei, *Angew. Chem. Int. Ed.,* **2015**, *54*, 1791-1794.
53. J. Ma, and L.-W. Wang, *Nano Lett.*, 2015, **15**, 248-253.
54. F. Brivio, A. B. Walker and A. Walsh, *APL Mater.*, 2013, **1**, 042111.
55. F. Brivio, K. T. Butler, A. Walsh and M. van Schilfgaarde, *Phys. Rev. B*, 2014, **89**, 155204.

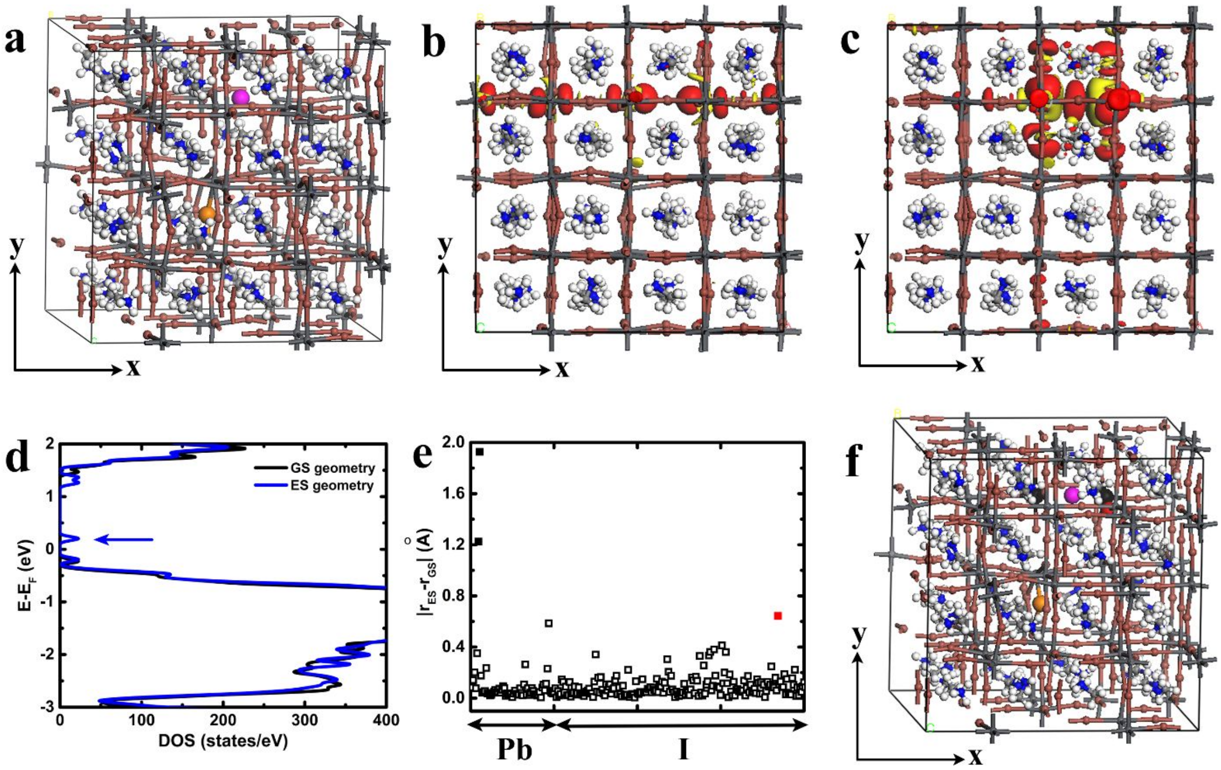

Figure 1. Effects of photoexcitation in MAPbI$_3$-FD1. (a) The positions of one Frenkel pair in MAPbI$_3$-FD1. The ion in magenta represents the position of V_I^+ defect and the ion in orange represents the position of I_i^- defect. (b) Lowest excited-state charge densities of MAPbI$_3$-FD1 in the ground-state (GS) geometry. (c) Lowest excited-state charge densities of MAPbI$_3$-FD1 in the excited-state (ES) configuration. In (b) and (c), the electron (hole) density is shown in red (yellow) and the value of iso-surface is 2.0×10^{-3} e Å^{-3}. (d) DOS of MAPbI$_3$-FD1 in both the ground-state and excited-state geometries. The discrete trap state is highlighted with the arrow. (e) Atomic displacements in MAPbI$_3$-FD1 from the ground-state geometry in (b) to the excited-state geometry in (c). (f) The ions with the largest displacements. Pb^{2+} ions (solid black) and I$^-$ ions (solid red) in (e) are shown with the same color.

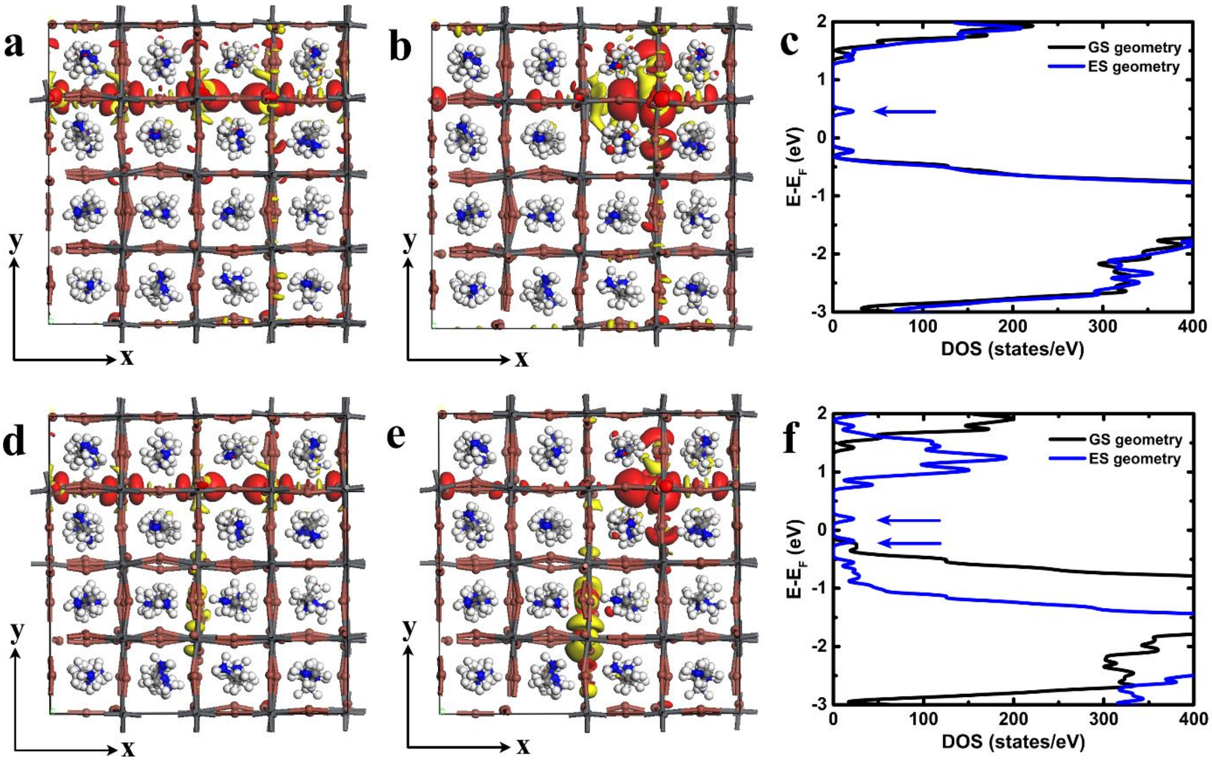

Figure 2. Charge densities and DOS in MAPbI$_3$-FD1. (a)-(b) Lowest excited-state charge densities of MAPbI$_3$-FD1 with I_i^- defect oriented by the nearest -NH$_3$ moieties of MA cations in ground-state and excited-state geometries, respectively. (c) DOS of ground-state geometry in (a) and excited-state geometry in (b). (d)-(e) Lowest excited-state charge densities of MAPbI$_3$-FD1 with I_i^- defect oriented by the nearest -CH$_3$ groups of MA cations in ground-state and excited-state geometries, respectively. (f) DOS of ground-state geometry in (d) and excited-state geometry (e). The discrete in-gap states are highlighted with the arrows in (c) and (f). The electron (hole) density is shown in red (yellow) and the value of iso-surface is 2.0×10^{-3} e Å^{-3} in (a), (b), (d) and (e).

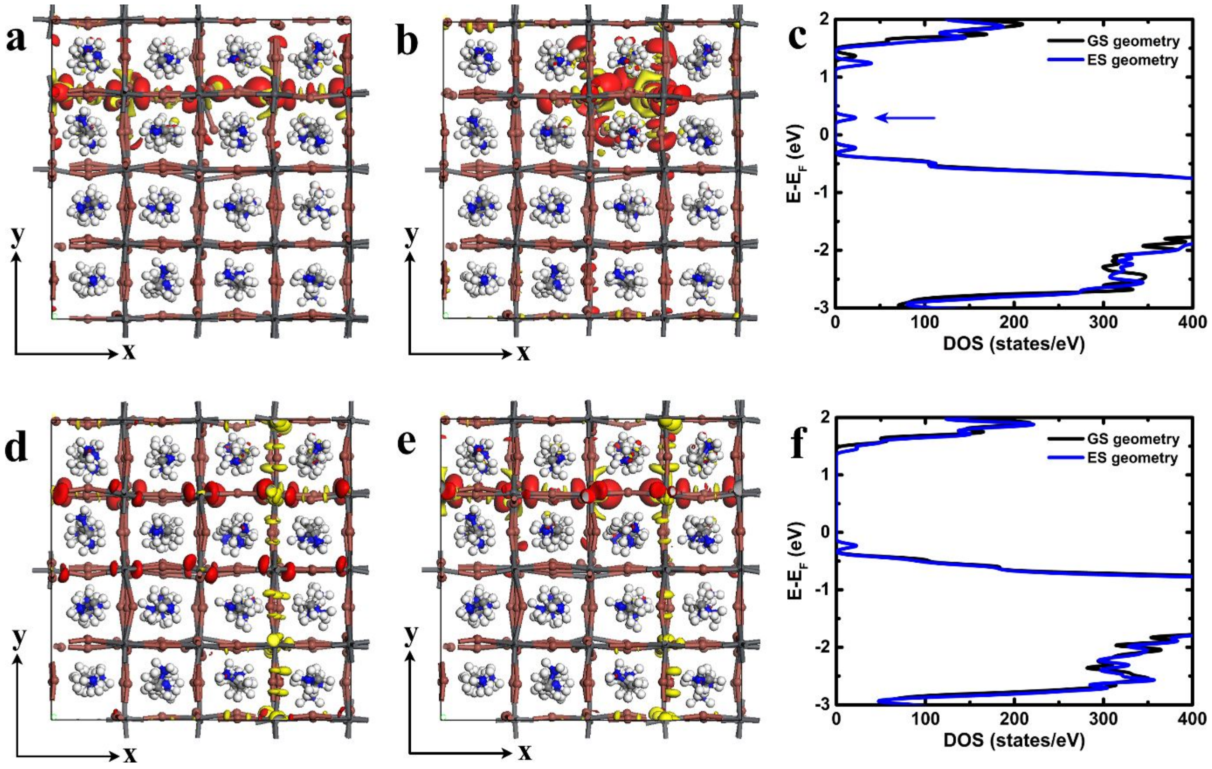

Figure 3. Charge densities and DOS in MAPbI$_3$-FD1. (a)-(b) Lowest excited-state charge densities of MAPbI$_3$-FD1 with V_I^+ defect oriented by the nearest -NH$_3$ groups of MA cations in ground-state and excited-state geometries, respectively. (c) DOS of ground-state geometry in (a) and excited-state geometry in (b). (d)-(e) Lowest excited-state charge densities of MAPbI$_3$-FD1 with V_I^+ defect oriented by the nearest -CH$_3$ moieties of MA cations in ground-state and excited-state geometries, respectively. (f) DOS of ground-state geometry in (d) and excited-state geometry in (e). The discrete in-gap state in (c) is highlighted with the arrow. The electron (hole) density is shown in red (yellow) in (a) (b), (d) and (e). The value of iso-surface is 2.0×10^{-3} e Å^{-3} in (a) and (b) as well as 1.0×10^{-3} e Å^{-3} in (d) and (e).

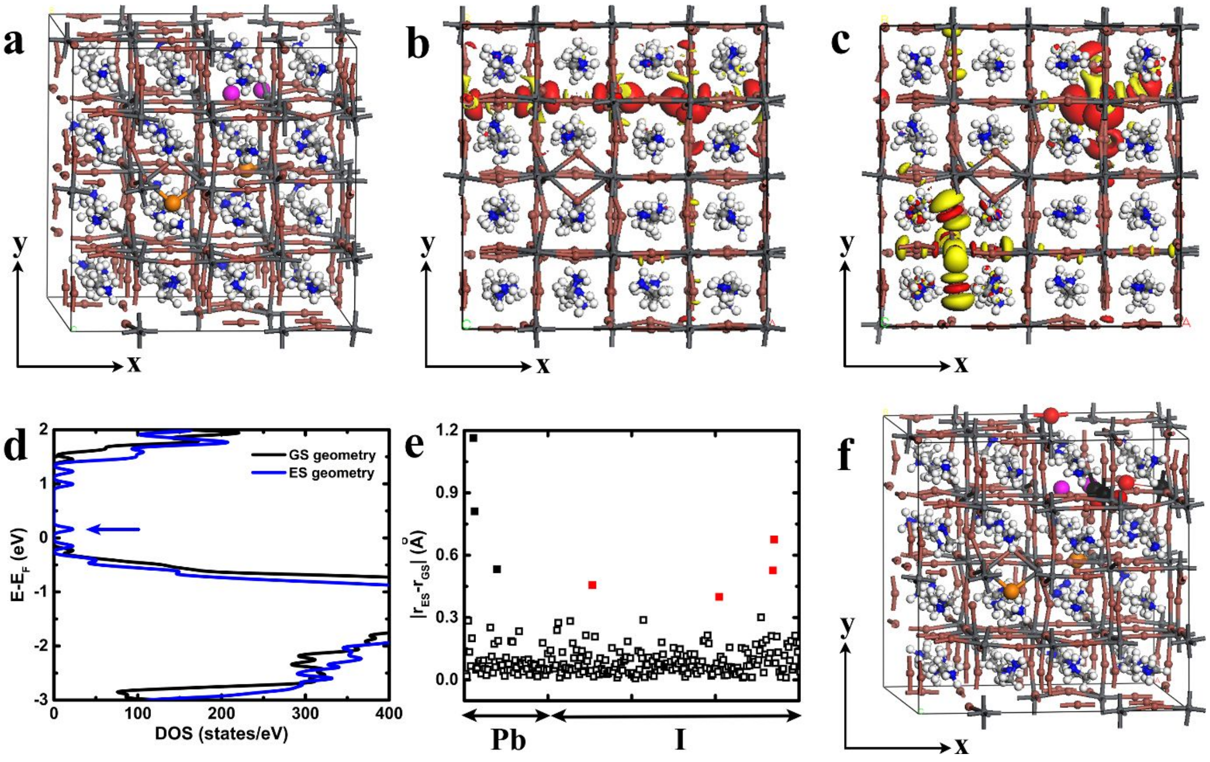

Figure 4. Effects of photoexcitation on $MAPbI_3$-FD2. (a) The positions of two Frenkel pairs in $MAPbI_3$-FD2. The ions in magenta represent the position of V_I^+ defects and the ions in orange represent the position of I_i^- defects. (b) Lowest excited-state charge densities of $MAPbI_3$-FD2 in ground-state geometry. (c) Lowest excited-state charge densities of $MAPbI_3$-FD2 in excited-state configuration. In (b) and (c), the electron (hole) density is shown in red (yellow) and the value of iso-surface is 2.0×10^{-3} e $Å^{-3}$. (d) DOS of $MAPbI_3$-FD2 in both the ground-state and excited-state geometries. The discrete trap state is highlighted with the arrow. (e) Atomic displacements in $MAPbI_3$-FD2 from the ground-state geometry in (b) to the excited-state geometry in (c). (f) The ions with the largest displacements. Pb^{2+} ions (solid black) and I^- ions (solid red) in (e) are shown with the same color.

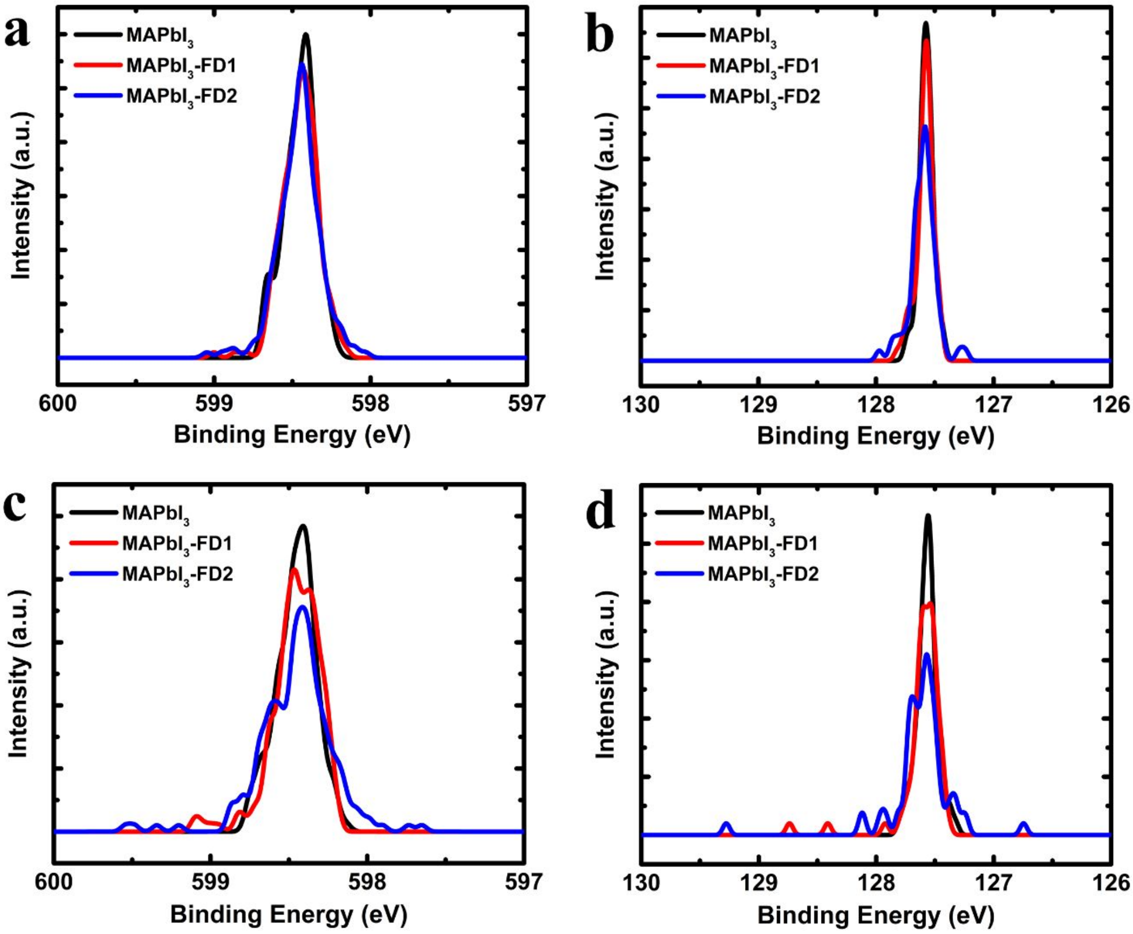

Figure 5. DFT-calculated core-level energies of pristine and defective $MAPbI_3$. (a) I 3d core-level energies for pristine $MAPbI_3$, $MAPbI_3$-FD1 and $MAPbI_3$-FD2 in the ground-state geometries. (b) Pb 4f core-level energies for pristine $MAPbI_3$, $MAPbI_3$-FD1 and $MAPbI_3$-FD2 in the ground-state geometries. (c) I 3d core-level energies for pristine $MAPbI_3$, $MAPbI_3$-FD1 and $MAPbI_3$-FD2 in the excited-state geometries. (d) Pb 4f core-level energies for pristine $MAPbI_3$, $MAPbI_3$-FD1 and $MAPbI_3$-FD2 in the excited-state geometries.

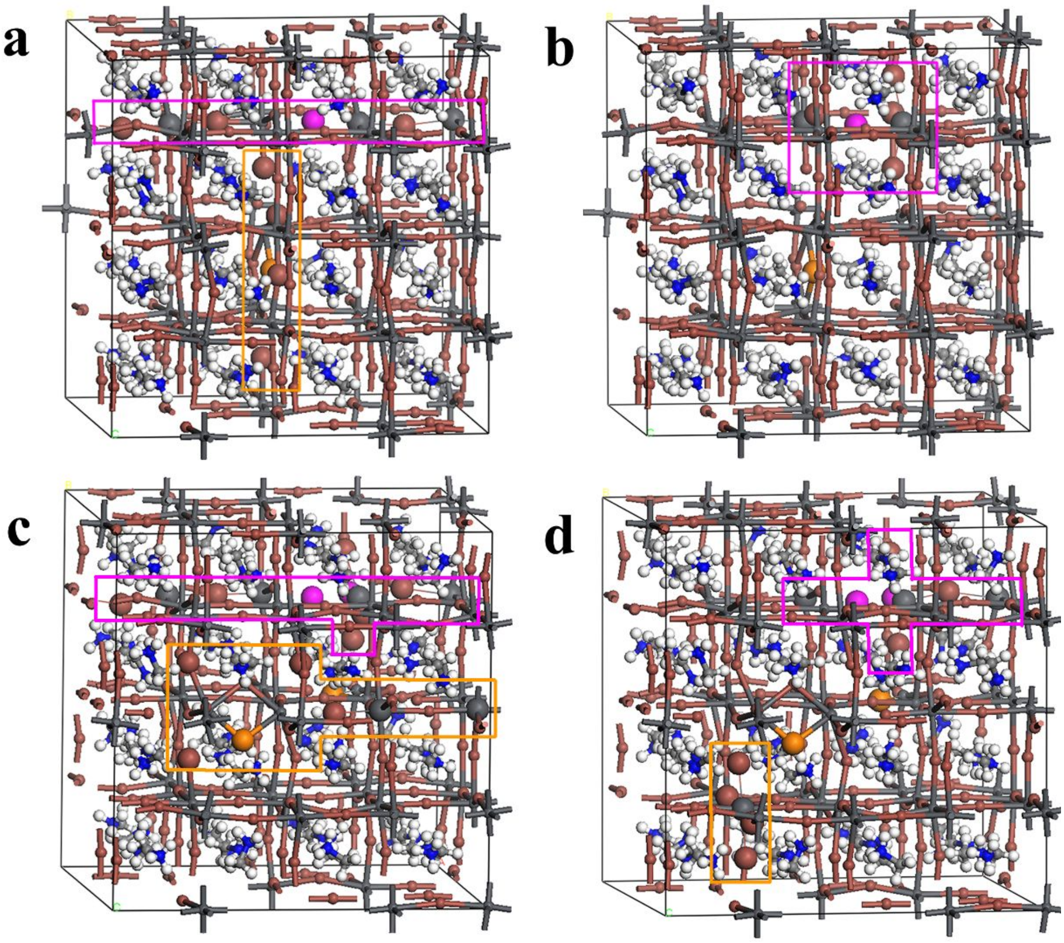

Figure 6. The charge transfer from pristine $MAPbI_3$ to defective $MAPbI_3$ in both the ground state and excited state. (a) Charge transfer in the ground-state configurations from pristine $MAPbI_3$ to $MAPbI_3$-FD1. (b) Charge transfer in the excited-state configurations from pristine $MAPbI_3$ to $MAPbI_3$-FD1. (c) Charge transfer in the ground-state configurations from pristine $MAPbI_3$ to $MAPbI_3$-FD2. (d) Charge transfer in the excited-state configurations from $MAPbI_3$ to $MAPbI_3$-FD2. The ions in magenta and in orange represent the positions of V_I^+ and I_i^- defects, respectively. The ions in larger size highlighted by the lines in magenta lose electrons, leading to the increase of binding energies in Figure 5. By contrast, the ions in larger size highlighted by the lines in orange obtain electrons, leading to the decrease of binding energies in Figure 5.